

RESEARCH PAPER

## Detection of Quasi-periodic Oscillations in SGR 150228213

To cite this article: Run-Chao Chen *et al* 2023 *Res. Astron. Astrophys.* **23** 085018

View the [article online](#) for updates and enhancements.

### You may also like

- [QUASI-PERIODIC OSCILLATIONS AND BROADBAND VARIABILITY IN SHORT MAGNETAR BURSTS](#)

Daniela Huppenkothen, Anna L. Watts, Phil Uttley et al.

- [Exploring a search for long-duration transient gravitational waves associated with magnetar bursts](#)

Ryan Quitzow-James, James Brau, James A Clark et al.

- [Searching for Quasi-periodic Oscillations in Astrophysical Transients Using Gaussian Processes](#)

Moritz Hübner, Daniela Huppenkothen, Paul D. Lasky et al.



# Detection of Quasi-periodic Oscillations in SGR 150228213

Run-Chao Chen, Can-Min Deng, Xiang-Gao Wang, Zi-Min Zhou, Xing Yang, Da-Bin Lin, Qi Wang, and En-Wei Liang  
Guangxi Key Laboratory for Relativistic Astrophysics, School of Physical Science and Technology, Guangxi University, Nanning 530004, China

dengcm@gxu.edu.cn, wangxg@gxu.edu.cn

Received 2023 April 17; revised 2023 May 18; accepted 2023 May 29; published 2023 July 11

## Abstract

The detection of quasi-periodic oscillations (QPOs) in magnetar giant flares (GFs) has brought a new perspective to studies of the mechanism of magnetar bursts. Due to the scarcity of GFs, searching for QPOs in magnetar short bursts is reasonable. Here we report the detection of a narrow QPO at approximately 110 Hz and a wide QPO at approximately 60 Hz in the short magnetar burst SGR 150228213, with a confidence level of  $3.35\sigma$ . This burst was initially attributed to 4U 0142+61 by Fermi/GBM on location, but we have not detected such QPOs in other bursts from this magnetar. We also found that there was a repeating fast radio burst associated with SGR 150228213 on location. Finally, we discuss the possible origins of SGR 150228213.

**Key words:** methods: statistical – (stars:) pulsars: individual (4U 0142+61) – X-rays: bursts

## 1. Introduction

Magnetars are a class of young neutron stars that have the strongest magnetic fields in the universe found so far. They have typical magnetic fields  $B \sim 10^{14}$  G, spin period  $P \sim 2\text{--}12$  s, and spin-down rate  $\dot{P} \sim 10^{-13}\text{--}10^{-11}$  s s<sup>-1</sup> (Turolla et al. 2015). These isolated neutron stars emit a wide array of electromagnetic radiation in radio, optical, X-ray, and gamma-ray bands by the decay of their enormous internal magnetic fields, which also yields the name “magnetar” (Duncan & Thompson 1992; Kaspi & Beloborodov 2017). Magnetars can be divided into soft gamma repeaters (SGRs) and anomalous X-ray pulsars (AXPs) judging from burst activities and other aspects.

Bursts from magnetars can be divided into three categories: short bursts are the most common type and have typical duration  $\sim 0.1$  s and peak luminosities  $\sim 10^{39}\text{--}10^{41}$  erg s<sup>-1</sup>; intermediate flares are rare events that usually last 1–40 s with peak luminosities  $\sim 10^{41}\text{--}10^{43}$  erg s<sup>-1</sup>; giant flares (GFs) are the most violent and unusual activities in magnetars and have an extremely bright hard peak lasting 0.1–0.2 s with a luminosity of  $10^{44}\text{--}10^{47}$  erg s<sup>-1</sup>, which is usually followed by a long pulsating tail lasting a few hundred seconds and modulated by the magnetar spin period (Turolla et al. 2015). Only four such GFs have been confirmed: GRB 790305 from SGR 0526-66 (Mazets et al. 1979; Cline et al. 1980), GRB 980827 from SGR 1900+14 (Feroci et al. 1999; Hurley et al. 1999; Mazets et al. 1999), GRB 041227 from SGR 1806-20 (Cameron et al. 2005; Gaensler et al. 2005; Hurley et al. 2005; Palmer et al. 2005), and GRB 200415A (Yang et al. 2020; Zhang et al. 2020; Roberts et al. 2021; Svinkin et al. 2021).

The associated events of SGR 1935+2154 and FRB 200428 on 2020 April 28 (Lin et al. 2020b; Bochenek et al. 2020;

CHIME/FRB Collaboration et al. 2020; Mereghetti et al. 2020; Li et al. 2021; Ridnaia et al. 2021) had established that at least some fast radio bursts (FRBs) are produced during magnetar bursts (Lyubarsky 2014, 2021; Katz 2016; Yang & Zhang 2018; Yu et al. 2021), but the mechanism behind these phenomena is unclear. Starquakes have been invoked to explain the occurrence of hard X-ray bursts and FRBs from magnetars (Thompson & Duncan 1995; Wang et al. 2018a). This kind of crustal oscillation would leave imprints in the form of quasi-periodic oscillations (QPOs) in the temporal profiles of magnetar bursts (Huppenkothen et al. 2014b; Miller et al. 2019).

QPOs have been found during the pulsating tails and the main peak of magnetar GFs (Barat et al. 1983; Israel et al. 2005; Strohmayer & Watts 2005, 2006; Castro-Tirado et al. 2021), and have also been found in some short bursts from SGRs (Huppenkothen et al. 2014a, 2014c; Li et al. 2022). These investigations have opened up the possibility of studying magnetars using asteroseismology (Huppenkothen et al. 2013). At present, due to the scarcity of GFs, searching for QPOs from short bursts is reasonable, although the duration of short bursts would limit the minimum frequency for such a search (Huppenkothen et al. 2013). In this paper we conduct a comprehensive analysis of SGR 150228213 and report the detection of a (quasi-)periodic signal in this burst. The structure of this paper is as follows. In Section 2 we describe the Bayesian framework for searching for (quasi-)periodic signals in the observed periodogram of magnetar bursts and estimating the significance. Section 3 is the periodogram analysis of SGR 150228213. We describe how to select samples and choose the appropriate time interval to conduct such analysis. We also discuss the results of (quasi-)periodic research in this section.

In Section 4 we discuss possible origins of SGR 150228213 and Section 5 is a summary of this work.

## 2. Methods for Periodogram Analysis

### 2.1. Generate the Periodogram

The observed periodogram analyzed in this work is based on the fast Fourier transform (FFT) of the light-curve data from the selected time interval. Powers in observed periodogram correspond to the squared Fourier transform of the data, and we make use of the stingray Python package (Huppenkothen et al. 2019) to perform this conversion to get the Leahy-normalized periodograms.

A periodogram generated from a pure noise process can be seen as the conversion of a stochastic time series. It is well known that the periodogram of any stochastic time series of length  $N$ , denoted  $I_j = I(f_j)$  at Fourier frequency  $f_j = j/N\Delta T$  (with  $j = 1, \dots, N/2$ ), is exponentially distributed about the true spectral density  $S_j = S(f_j)$ :

$$p(I_j|S_j) = \frac{1}{S_j} \exp(-I_j/S_j) \quad (1)$$

(Groth 1975; Leahy et al. 1983; Timmer & Koenig 1995). Thus we sampled the exponential distribution corresponding to the model power to generate (see Vaughan 2010) the simulated periodograms in this work.

### 2.2. Model the Periodogram

There are two alternative approaches to modeling the periodogram: one relies on models of the original light curve to generate the periodogram, the other uses the models of the observed periodogram directly. Modeling the original light curve is based on an accurate understanding of the burst mechanism, otherwise artificial model selection would have an immeasurable impact on potential QPO detection. Owing to the unknown emission mechanism of magnetar bursts, we chose to model the observed periodogram generated from the original light curve to search for (quasi-)periodic signals in magnetar bursts.

While modeling the observed periodogram, we made a simple but conservative assumption that all broadband powers in the periodogram are supplied by a noise process without QPO, which is the combination of red noise at low frequencies and white noise at high frequencies (Huppenkothen et al. 2013). Based on this assumption, searching for (quasi-)periodic signals through periodogram research can be followed by the Bayesian approach developed by Vaughan (2010); such a method provides a statistically rigorous framework to test whether additional model components (such as Lorentzian QPOs) are required by the data. And as was stated in Castro-Tirado et al. (2021), such an assumption will cause weak signals at low frequencies to be buried in the higher variance of

the broadband noise but would yield a very low false-positive detection rate in return.

A theoretical pure red-noise profile follows a broken power-law model, but in many cases the break frequency is relatively low, and the red-noise profile would be fitted better by the power-law model (Belli 1992; Lazzati 2002). Therefore, we need to select the preferred noise model of the observed periodogram from these two nested models below. We defined the PL model as a red-noise power-law function plus a white-noise (Poisson noise) constant as

$$P(\nu) = A\nu^{-\alpha} + C, \quad (2)$$

where  $\nu$  is the frequency,  $P(\nu)$  is the power,  $A$  is the amplitude,  $\alpha$  is the power-law index, and  $C$  is the constant representing the white-noise level. The BPL model is the combination of a broken power law and a white-noise constant, which is described as

$$P(\nu) = N \left[ 1 + \left( \frac{\nu}{\nu_b} \right)^\beta \right]^{-1} + C, \quad (3)$$

where  $N$  is the normalization value,  $\nu_b$  is the break frequency, and  $\beta$  is the power-law index after  $\nu_b$ .

As for the model fitting, we obtained the optimum model parameter set from the maximum a posteriori estimates, which could be computed by minimizing the maximum likelihood estimation (MLE) function (Vaughan 2010; Huppenkothen et al. 2013)

$$D(\mathbf{I}, \boldsymbol{\theta}, H) = -2 \log p(\mathbf{I}|\boldsymbol{\theta}, H) = 2 \sum_{j=1}^{N/2} \left\{ \frac{I_j}{S_j} + \log S_j \right\}, \quad (4)$$

where  $p(\mathbf{I}|\boldsymbol{\theta}, H) = \prod_{j=1}^{N/2} p(I_j|S_j)$  is the joint likelihood function,  $I_j$  is the individual power in the observed periodogram, and  $S_j$  is the power in the noise model for a parameter set  $\boldsymbol{\theta}$ .

To select the preferred noise model, we make use of the likelihood ratio test (LRT). The *null hypothesis* is that the periodogram can be described by a simple model, PL ( $H_0$ ); then we estimated whether the  $H_0$  model could be replaced by a more complex model, BPL (the alternative hypothesis,  $H_1$ ) through the LRT statistic

$$\begin{aligned} T_{\text{LRT}} &= -2 \log \frac{p(\mathbf{I}|\hat{\boldsymbol{\theta}}_{\text{MLE}}^0, H_0)}{p(\mathbf{I}|\hat{\boldsymbol{\theta}}_{\text{MLE}}^1, H_1)} \\ &= D_{\min}(H_0) - D_{\min}(H_1). \end{aligned} \quad (5)$$

We can generate  $n$  sets of simulated periodograms by sampling the posterior distribution of  $H_0$  model parameters. We then compute the corresponding  $T_{\text{LRT}}$  by fitting each fake periodogram with both  $H_0$  and  $H_1$  models. The preferred noise model can be judged from the tail area probability ( $p$ -value) of the observed  $T_{\text{LRT}}$  in the distribution of the simulated  $T_{\text{LRT}}$ . It is necessary to emphasize that this test cannot be seen as direct evidence in favor of the  $H_1$  model (usually the more complex

one), but only strictly as evidence against the  $H_0$  model (Huppenkothen et al. 2014c).

### 2.3. Search for (Quasi-)periodic Signals

After the selection of the preferred noise model, we use it to search for periodic signals or QPO candidates. We computed residuals of the observed power to noise model power in the logarithmic periodogram from the selected noise model with the optimum parameter set. Such a residual is equivalent to  $I_j/S_j$ , for which we can use the  $T_R$  statistic to estimate the chance probability of the candidates.  $T_R$  is the maximum ratio of observed to model power given by

$$T_R = \max(\hat{R}_j), \quad (6)$$

where

$$\hat{R}_j = 2I_j/S_j. \quad (7)$$

In this step, we generated  $n$  sets of simulated periodograms by sampling the posterior distribution of the selected noise model parameters; from each periodogram we could obtain the new  $T_R$ . These statistics would be distributed as  $\chi^2$  and we can get the  $p$ -value of  $T_R$  by computing the tail area probability (Vaughan 2010; Huppenkothen et al. 2013).

The search for QPOs in the observed periodogram is similar to the selection of a noise model. In this step, the null hypothesis,  $H_0$ , becomes that the periodogram can be well described by the selected noise model, and the alternative hypothesis,  $H_1$ , model is the superposition of the  $H_0$  noise model and one or several Lorentz lines to account for QPOs (Castro-Tirado et al. 2021). A Lorentz line is described by (Arnaud 1996)

$$P(\nu) = K(\sigma/2\pi)/[(\nu - \nu_p)^2 + (\sigma/2)^2], \quad (8)$$

where  $K$  is the normalization factor,  $\sigma$  is the FWHM of the line, and  $\nu_p$  is the centroid frequency of QPO. We can take the  $p$ -value of the  $H_1$  model obtained by LRT statistics as the significance of such QPO based on the establishment of  $H_0$ .

## 3. Periodogram Analysis for SGR 150228213

### 3.1. Sample Selection

Fermi/GBM is an all-sky monitor for any burst event and covers the energy range from 8 keV to 40 MeV (Meegan et al. 2009), which is suitable for the detection of short bursts from magnetars. After years of accumulation, we have collected information on 524 bursts that were classified as SGR by machine from the official website of Fermi<sup>1</sup>; 177 of them are certified from known sources and the other 347 bursts are certified from unknown sources.

Studies of magnetar bursts based on the observation data from Fermi/GBM usually target specific magnetars for batch

analysis, and especially for those active SGRs, e.g., SGR 1935+2154 (Lin et al. 2020a) and SGR 1550-5418 (Huppenkothen et al. 2014c). In this work, we focused on those bursts that were certified from unknown sources and preferred those associated with known magnetars or FRBs (sources), which are more likely to originate from magnetars. Therefore, we compared the location information for the 347 bursts from unknown sources with 30 magnetars from the McGill Magnetar Catalog<sup>2</sup> (Olausen & Kaspi 2014) and 626 FRBs from the CHIME/FRB catalog<sup>3</sup> (CHIME/FRB Collaboration et al. 2021), FRBCAT<sup>4</sup> (Petroff et al. 2016), and the Transient Name Server.<sup>5</sup> After the comparison, except for the samples associated with SGR 1935+2154, we found only one burst, SGR 150228213, that is related to a known magnetar, AXP 4U 0142+61, and a repeating FRB source, FRB 180916, on location.

However, 4U 0142+61 is not associated with FRB 180916, but the periodogram analysis for SGR 150228213 has revealed a possible periodic or quasi-periodic signal. The later content of this section describes our periodogram analysis for SGR 150228213 and estimation of the significance of related results; two different origins will be discussed in Section 4.

### 3.2. Light curve Analysis

Considering that short bursts from magnetars usually have short duration and a soft energy spectrum, we combined the time-tagged event data files from all triggered NaI detectors (n4, n8) and rebinned the data to 2 ms time resolution to analyze the light curve in the energy range 8–100 keV.

We use  $T_{90}$  to describe the main part of this burst, which is the time interval within which the accumulated counts of the burst increase from 5% to 95% of the total counts (Kouveliotou et al. 1993). Since the estimation of  $T_{90}$  will be affected by background level, and SGR 150228213 was triggered during the active phase of 4U 0142+61, which had caused the background to fluctuate greatly, we selected a relatively long time interval near the burst to estimate the average background level in order to neutralize the effects of some potentially weak bursts; this is the time intervals from −25 s to −1 s and 1–25 s relative to the trigger time  $T_0$ . The light curve from −0.2 to 0.2 s is shown in Figure 1, in which we also plot the accumulated net counts corresponding to the light curve. The  $T_{90}$  we computed is ∼98 ms.

In addition, to depict the local characteristics of the burst and select a suitable interval to conduct the periodogram research, we adopted the Bayesian blocks algorithm described in Scargle et al. (2013) to analyze the light-curve data from −25 s to 25 s relative to  $T_0$  in the same time resolution. The accumulated net

<sup>2</sup> <https://www.physics.mcgill.ca/pulsar/magnetar/main.html>

<sup>3</sup> <https://www.chime-frb.ca>

<sup>4</sup> <https://www.frbcat.org>

<sup>5</sup> <https://www.wis-tns.org>

<sup>1</sup> <https://fermi.gsfc.nasa.gov>

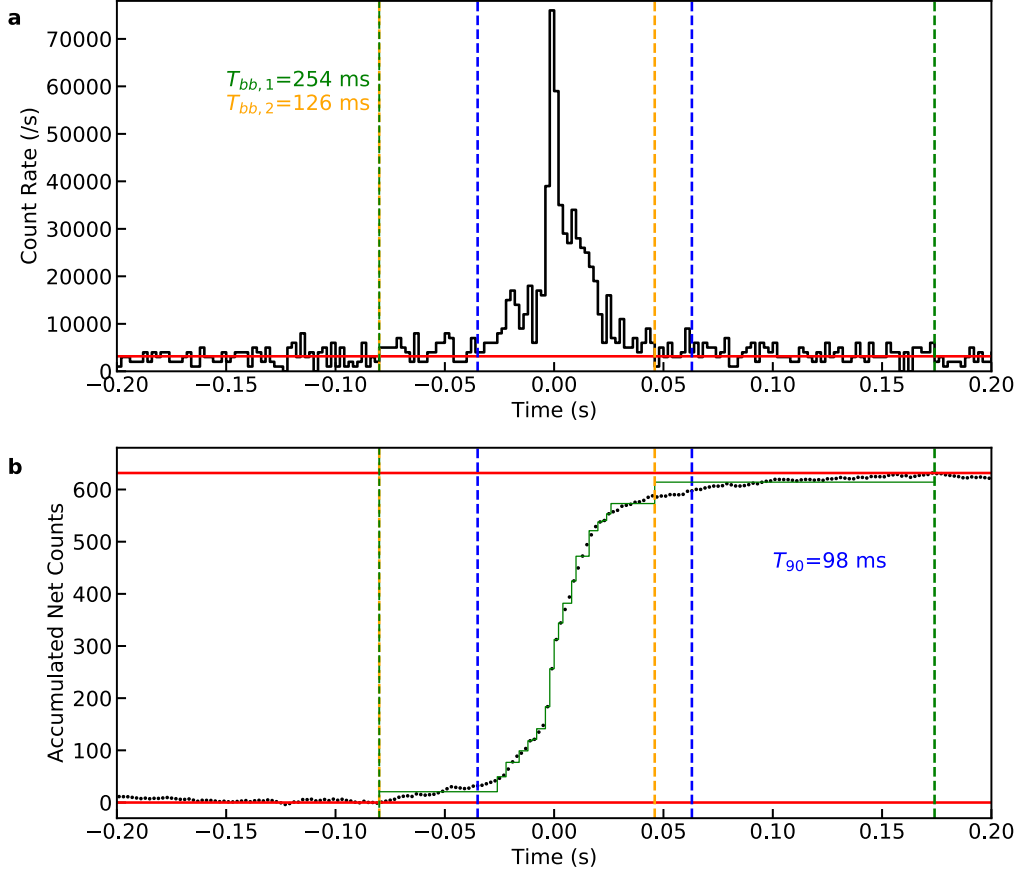


**Figure 1.** Light curve of SGR 150228213. (a) The black solid line represents the light curve obtained from the combination of events data from detectors n4 and n8 in 8–100 keV. The red solid line shows the background level. (b) The black points represent the variation in accumulated counts, and the red solid lines show the 0% and 100% levels of the total accumulated counts. The two regions marked by the blue and yellow vertical dashed lines are the  $T_{90}$  and Bayesian block time ( $T_{bb,2}$ ) intervals of the light curve; the time interval  $T_{bb,1}$  within green vertical dashed lines is the total burst duration we select to conduct the periodogram research.

counts of each “block” are also drawn in Figure 1 in the form of a ladder graph. For the light curve in Figure 1 that includes the total duration to calculate  $T_{90}$  of the burst, there is a long “block” covers the 95% and 100% points of the total accumulated net counts. According to the description in Yang et al. (2021), the Bayesian block duration time  $T_{bb}$  for bursts from magnetar SGR 1935+2156 has a power-law trend with  $T_{90} \propto T_{bb}^{0.91 \pm 0.05}$ . Following this correlation,  $T_{bb,2} \sim 126$  ms in Figure 1 is the suitable Bayesian block duration of SGR 150228213. However, since the interval  $T_{bb,2}$  does not contain the main part of the burst ( $T_{90}$ ), we treat the interval  $T_{bb,1}$  (−80 ms to 174 ms relative to  $T_0$ ) as the total duration of SGR 150228213 for periodogram analysis; this contains the main part of the burst and the part that could not be distinguished as burst or background.

### 3.3. Periodogram Analysis

According to temporal analysis of SGR 150228213, we select two different time segments to compute the observed

periodograms: the interval from −80 ms to 174 ms relative to  $T_0$  denotes the total duration of the burst based on Bayesian blocks, and the interval from −44.8 ms to 72.8 ms relative to  $T_0$  is the burst duration based on  $T_{90}$ , refer to Huppenkothen et al. (2013). We combined the event data from all detectors in 8–100 keV and rebinned the light-curve data to 0.2 ms time resolution (corresponding to a Nyquist frequency of 2500 Hz).

Referring to Huppenkothen et al. (2014c), the specific process for noise model selection and the LRT statistic is as follows.

1. We made use of the Python package emcee (Foreman-Mackey et al. 2013) to perform a suit of Markov Chain Monte Carlo simulations (MCMCs) and sampled the posterior predictive distribution of the  $H_0$  model (PL) with 50 MCMC ensemble walkers and 1000 samples for each walker (containing 20% of samples in the burn-in phase for each walker).
2. We simulated 1000 sets of periodograms from the MCMC sample of the PL model and fit each periodogram

**Table 1**  
Preferred Noise Model and Potential Periodicities in SGR 150228213

Time Interval (ms)	Model	Noise Model Selection			Search for Periodicities		
		$T_{\text{LRT}}^{\text{BPL}}$	$p(\text{LRT})$	Boundary (Hz)	Frequency (Hz)	$T_R$	$p(T_R)$
−80 to 174	PL	−5.22	0.881	118.22	114.17	13.13	0.021
					1590.55	11.55	0.853
−44.8 to 72.8	PL	−5.55	0.947	159.88	110.54	9.98	0.075
					1590.14	11.81	0.522

**Table 2**  
Parameter Posteriors and Chance Probabilities for Potential QPOs in SGR 150228213

Time Interval (ms)	Noise Model		Search for QPOs					
	$(H_0)$	$D_{\min}(H_0)$	Frequency (Hz)	FWHM (Hz)	Norm	$D_{\min}(H_1)$	$T_{\text{LRT}}^{\text{obs}}$	$p(\text{LRT})$
−80 to 174	PL	1700.56	112.20 $^{+1.02}_{-1.02}$	5.64 $^{+3.95}_{-3.50}$	162.18 $^{+2.29}_{-2.14}$	1694.44	6.12	0.0008
			57.54 $^{+1.12}_{-1.15}$	26.84 $^{+31.36}_{-17.41}$	594.54 $^{+1.58}_{-1.45}$	1691.94	8.63	0.0004
			112.20 $^{+1.02}_{-1.02}$	4.80 $^{+4.49}_{-3.07}$	173.78 $^{+2.13}_{-2.40}$			
−44.8 to 72.8	PL	791.82	109.64 $^{+1.05}_{-1.05}$	10.98 $^{+9.43}_{-6.98}$	295.12 $^{+2.40}_{-2.95}$	788.42	3.29	0.0058
			61.66 $^{+1.29}_{-1.23}$	33.40 $^{+54.72}_{-22.13}$	1000.00 $^{+1.86}_{-2.14}$	790.05	1.77	0.0032
			109.65 $^{+1.05}_{-1.05}$	7.21 $^{+3.22}_{-4.36}$	218.78 $^{+2.57}_{-3.02}$			

with PL and BPL models to compute the distribution of  $T_{\text{LRT}}$  for those fake periodograms.

3. If the  $p$ -value of rejecting the PL model ( $H_0$ ) from the observed periodogram falls below 0.05, we selected the BPL model as the preferred noise model. Otherwise, we preserve the PL model as the preferred one.

After selection of the noise model, we found that the preferred noise model of both segments is PL. We then use the PL model with optimum parameter set to calculate a boundary frequency between the red-noise-dominated part and the white-noise-dominated part through  $\nu = (A/C)^{1/\alpha}$ . Divided by this boundary, we can compute  $T_R$  in each part on the observed periodogram and obtain the corresponding (quasi-)periodic candidates. Using the MCMC sample of the PL model, we simulated 1000 sets of periodograms to compute the distribution of  $T_R$  in each part on the fake periodograms and then estimate the corresponding  $p$ -value of each candidate.

Results for noise model selection and periodic research in different time segments are presented in Table 1. It can be seen that there might be a possible periodic signal or QPO candidate at  $\sim 110$  Hz for each observed periodogram, which is located within the red-noise-dominated part. The signal with minimum  $p(T_R)$  appears in the time interval from −80 ms to 174 ms.

Considering that these candidates could be a narrow QPO signal at  $\sim 110$  Hz, we add one Lorentz line to the PL model as a new  $H_1$  model to fit the observed periodograms in each time segment. The frequency of each QPO candidate is set as the

initial value of the centroid frequency of the Lorentz line, and the width of this QPO was limited within a very narrow range (less than three times the minimum frequency in each periodogram). As can be seen from Table 2, the centroid frequency of this narrow QPO we suspect in all segments is still at about 110 Hz. We then drew 5000 sets of simulated periodograms from the MCMC sample of the PL model (new  $H_0$  for QPO research) to compute the distribution of LRT statistics from PL and PL+QPO models; such a QPO with the lowest  $p$ -value (the tail area fraction of  $T_{\text{LRT}}^{\text{obs}}$ ) of  $\sim 0.0008$  exists in the interval from −80 ms to 174 ms, which is also consistent with the result above.

Figure 2 is the periodogram of the observed data from −80 ms to 174 ms relative to  $T_0$  and the corresponding models with the optimum parameter sets in each step of the periodogram analysis. We noticed that there still exists a potential wide QPO signal at about 60 Hz. However, such a signal is not significant enough for the periodogram from −44.8 ms to 72.8 ms relative to  $T_0$  (Figure 3). In order to find this potential wide QPO, we continued to use the QPO model with two Lorentz lines as a new  $H_1$  model to fit the observed periodograms. In this case, we no longer restrict the width parameter for the wide QPO component but still set its initial centroid frequency at 110 Hz. We still use 5000 sets of simulated periodograms generated from the MCMC sample of the PL model to compute the distribution of LRT statistics and estimate the corresponding  $p$ -value of the new  $H_1$  model with a wide QPO and a narrow QPO. The fitting results corresponding to each time segment

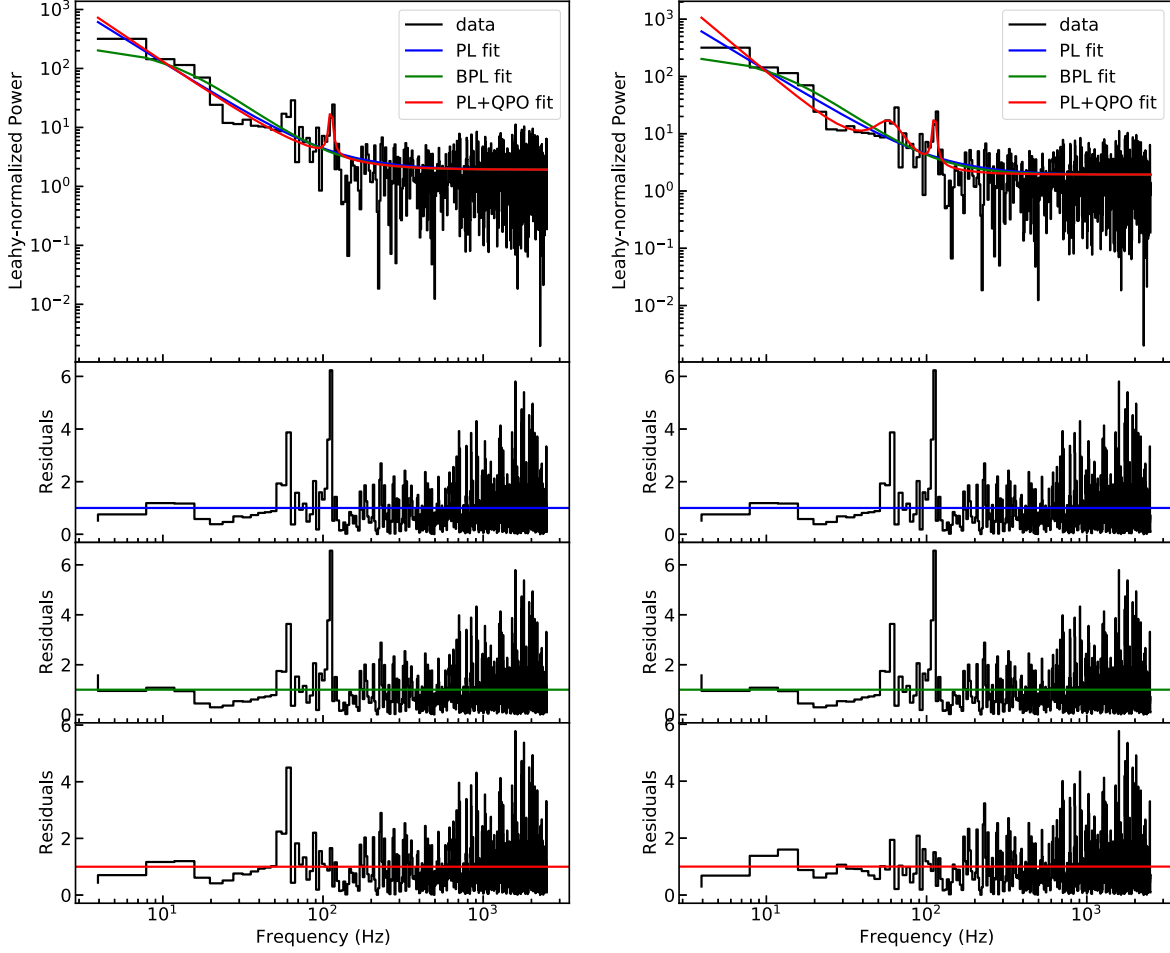


**Figure 2.** The observed periodogram from the time interval from  $-80$  ms to  $174$  ms relative to  $T_0$ . The left panel presents the diagram for the QPO model based on the assumption that the periodic signal is a potential QPO signal. The right panel presents the diagram for the model of a wide QPO at  $57.54$  Hz and a narrow QPO at  $112.20$  Hz.

are presented in Table 2. We can see that the frequency of the narrow QPO is still  $\sim 110$  Hz in the time intervals from  $-80$  to  $174$  ms and from  $-44.8$  to  $72.8$  ms, and the wide QPO component is located at approximately  $60$  Hz. The result with the lowest  $p$ -value of  $\sim 0.0004$  still exists in the interval from  $-80$  to  $174$  ms.

### 3.4. Duration of the QPOs

To depict the variation of QPOs we discovered in the burst light curve, we employed the Lomb–Scargle method (Lomb 1976; Scargle 1982) to analyze the detrended light curve of SGR 150228213 in  $8$ – $100$  keV. Considering the weak signal-to-noise ratio in some untriggered detectors, we only analyzed data from n4, n8, the combination of n4+n8, and the combination of all NaI detectors. A time window of length  $0.1$  s was used to produce Lomb–Scargle periodograms, which were combined into a spectrogram with time step of  $0.2$  ms.

The corresponding diagram is presented in Figure 4. The analysis for data combined from all NaI detectors is consistent with the detection of QPOs: the wide QPO at about  $60$  Hz appeared from about  $-0.06$  to  $0.05$  s, and the narrow QPO at about  $110$  Hz appeared from about  $-0.05$  to  $0.05$  s. Such QPOs are also visible in the results of n8 and the combination of n4 +n8, and we can see that the most significant result exists for the single detector n8. In addition, the result for n4 presented a continuous power excess or no support for the existence of QPOs.

From the results in Table 2, we can see that the significance is much lower in the shorter time interval centered on this burst, while we would usually expect the opposite behavior if the QPOs were a real property of the burst. However, as can be seen from Figure 4, the most significant QPOs appeared at about  $-0.05$  s, which may cause the lower significance in the shorter time interval. In addition, the centroid frequencies of these two QPOs seem to have a relation of an integral multiple,

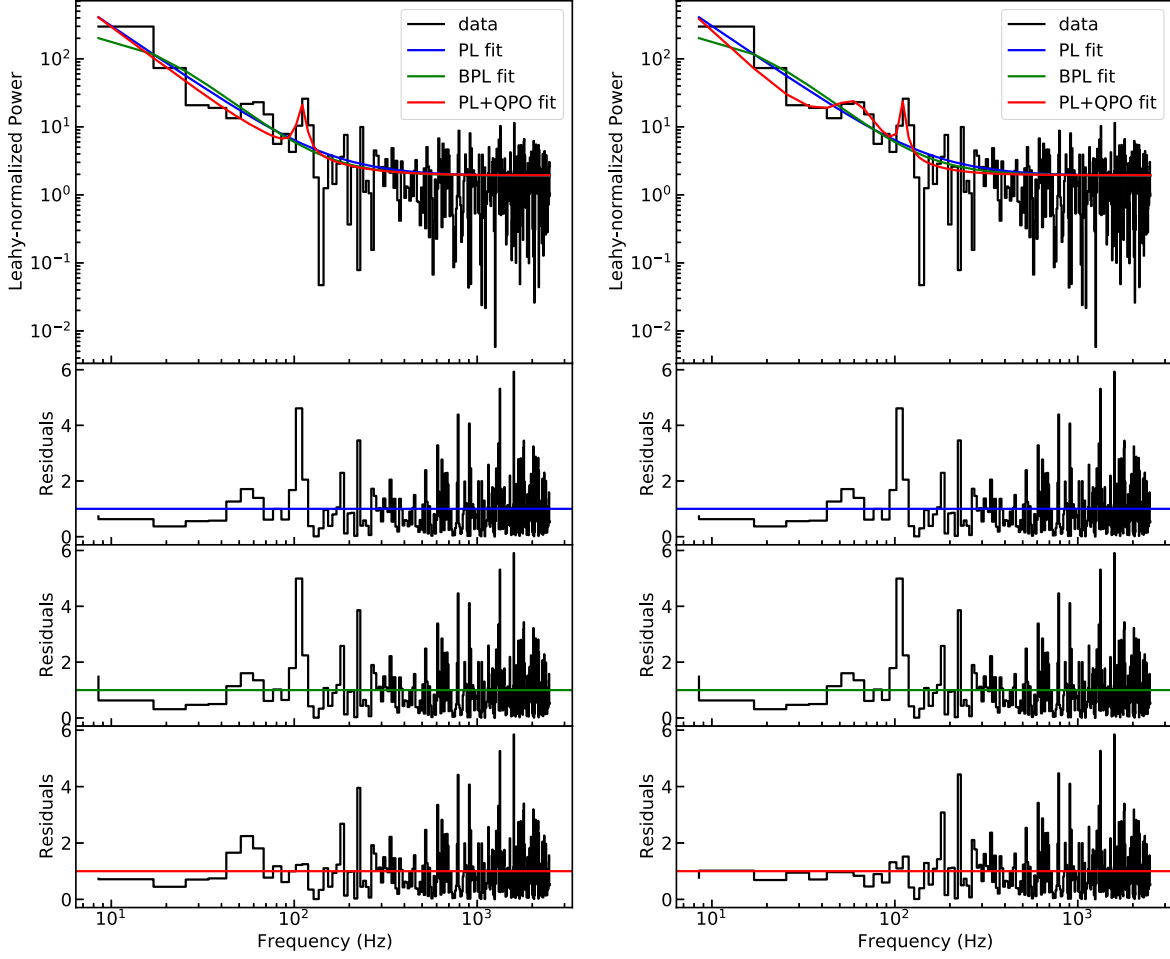


**Figure 3.** The observed periodogram from the time interval from  $-44.8$  ms to  $72.8$  ms relative to  $T_0$ . Both panels present a QPO at about 110 Hz, and the right panel presents the possible wide QPO at about 60 Hz.

which indicates that the high frequency of 110 Hz (or 120 Hz) might be the second harmonic of the 55 Hz (or 60 Hz) fundamental.

### 3.5. Gaussian Process Analysis

Gaussian processes (GPs) have been employed for searching QPOs in transient astrophysical events in recent years (Hübler et al. 2022; Xiao et al. 2022). The GP models QPOs as a stochastic process on top of a deterministic shape, and the latter can be understood as a mean model describing the overall trend of the burst light curve. Since the QPOs at about 60 and 110 Hz lie in the red-noise-dominated part and their confidence level was insufficient based on the noise model, we can use GPs to verify whether such QPOs are generated from the red-noise process in the time domain.

Following the procedure described in Hübler et al. (2022), we defined the kernel function describing a QPO as

$$k_{\text{qpo}}(\tau) = a \cos(2\pi f \tau) \exp(-c\tau), \quad (9)$$

where  $\tau$  is a time constant,  $a$  is the amplitude of the oscillation,  $f$  is its frequency, and  $c$  is the inverse of the decay time of the QPO. The kernel function describing the red noise is defined as

$$k_{\text{rn}}(\tau) = a \exp(-c\tau). \quad (10)$$

As the function for the mean model, since the physical mechanism of SGR 150228213 is unknown, we adopted three phenomenological models that can describe the trend of light curves for gamma-ray bursts (GRBs) or flares, i.e., skewed Gaussians, skewed exponentials, and FRED models (Norris et al. 1996; Huppenkothen et al. 2015; Hübler et al. 2022). The significance of the QPO can be described by the Bayes factor  $BF_{\text{qpo}}$ , defined as

$$BF_{\text{qpo}} = \frac{Z(d|k_{\text{qpo+rn}}, \mu)}{Z(d|k_{\text{rn}}, \mu)}, \quad (11)$$

where  $k_{\text{qpo+rn}} = k_{\text{qpo}}(\tau) + k_{\text{rn}}(\tau)$  is the kernel function describing the QPO and the red-noise process with different  $c$ ,  $Z(d|k_{\text{qpo+rn}}, \mu)$  and  $Z(d|k_{\text{rn}}, \mu)$  are the respective evidences in the QPO+red-noise and red-noise models,  $\mu$  is the parameter of the mean function, and  $d$  is the data.

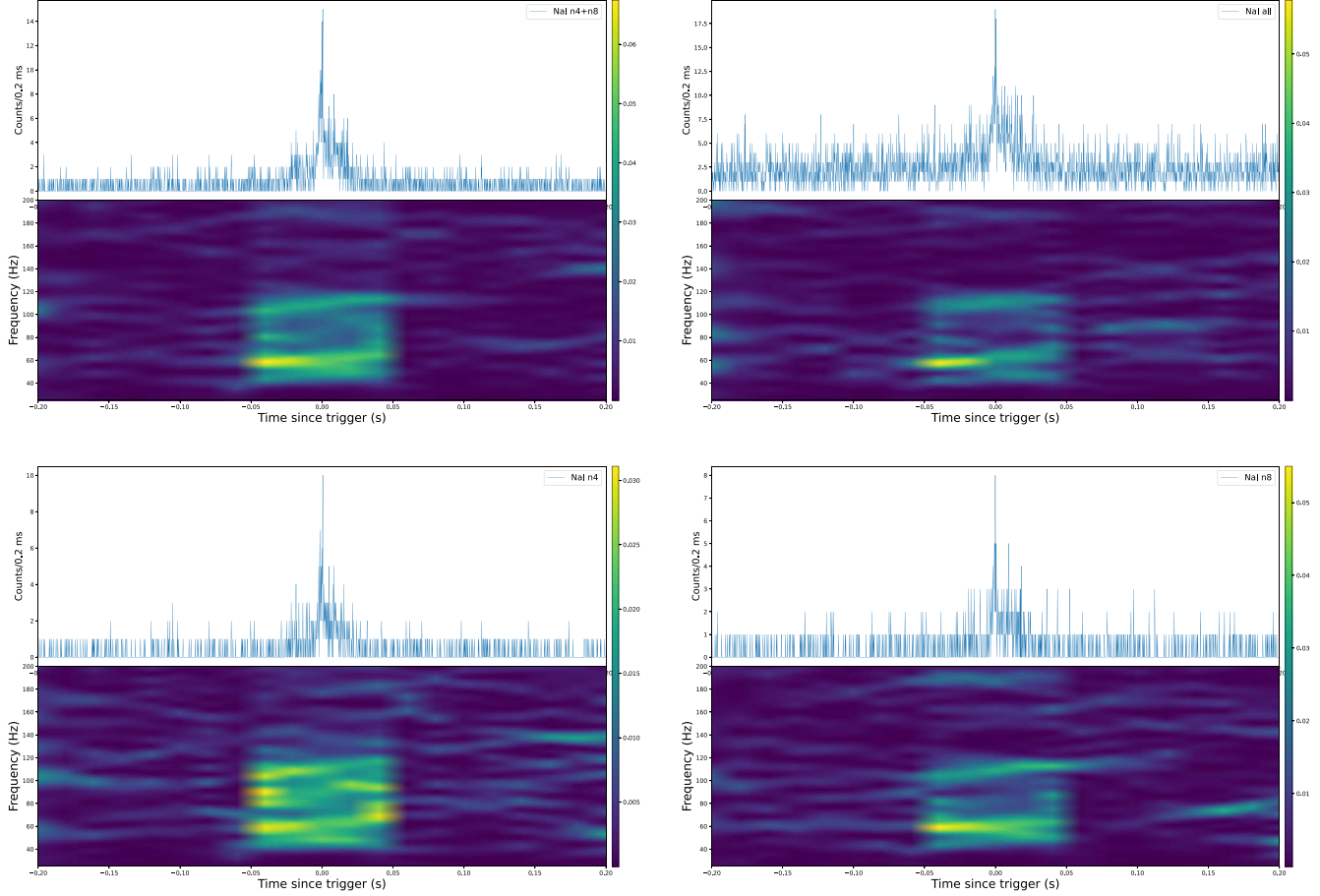


**Figure 4.** Lomb–Scargle periodogram analysis of SGR 150228213 between  $-0.2$  and  $0.2$  s. Different panels denote analysis of the detrended light curve from the combination of  $n4+n8$  (top left), the combination of all NaI detectors (top right), detector  $n4$  (bottom left), and detector  $n8$  (bottom right). The energy range is 8–100 keV and the time resolution is  $0.2$  ms.

In this section, we applied GPs to the light-curve data from the combination of all detectors in the time interval from  $-80$  to  $174$  ms relative to  $T_0$  with  $1$  ms time resolution, and we made use of the publicly available code<sup>6</sup> of GPs released by Hübner et al. (2022) to obtain the results. According to the results, the QPO is disfavored under the mean models of one FRED ( $\ln BF_{\text{qpo}} = -1.8$ ), two FREDs ( $\ln BF_{\text{qpo}} = -0.97$ ), and one skewed Gaussians ( $\ln BF_{\text{qpo}} = -0.78$ ). And the QPO is favored under one skewed exponential ( $\ln BF_{\text{qpo}} = 0.21$ ), two skewed exponentials ( $\ln BF_{\text{qpo}} = 3.02$ ), and two skewed Gaussians ( $\ln BF_{\text{qpo}} = 1.49$ ). The light curve under different mean models is presented in Figure 5, and the frequency posterior is presented in Figure 6. We found that the results of the analysis based on different mean models may (or may not) be favorable to the existence of QPOs, and the skewed exponentials performed better than other models for the burst profile if the Bayes factor is used for comparisons of mean models.

In addition, the QPO frequency posterior for SGR 150228213 is constrained in all models, and the results are consistent with the detection of QPOs through frequency domain analysis. As we concluded in Section 3.4, the QPO at about  $110$  Hz may be a second harmonic of the  $55$  Hz fundamental, and such a conjecture seems also supported by the frequency distributions in Figure 6. However, since the significance of such QPOs varies under different mean models, we reserve the results of frequency domain analysis as final judgment. We can see the potential of GPs for detecting QPOs in magnetar bursts; after all, the significance based on frequency domain analysis is usually recommended under the premise of infinitely long time series.

## 4. Discussion on Possible Origins of SGR 150228213

### 4.1. SGR 150228213 as a Magnetar Burst from 4U 0142+61

In the trigger report for SGR 150228213, Fermi/GBM attributed this burst to the activity of 4U 0142+61, and the

<sup>6</sup> <https://github.com/MoritzThomasHuebner/QPOEstimation>

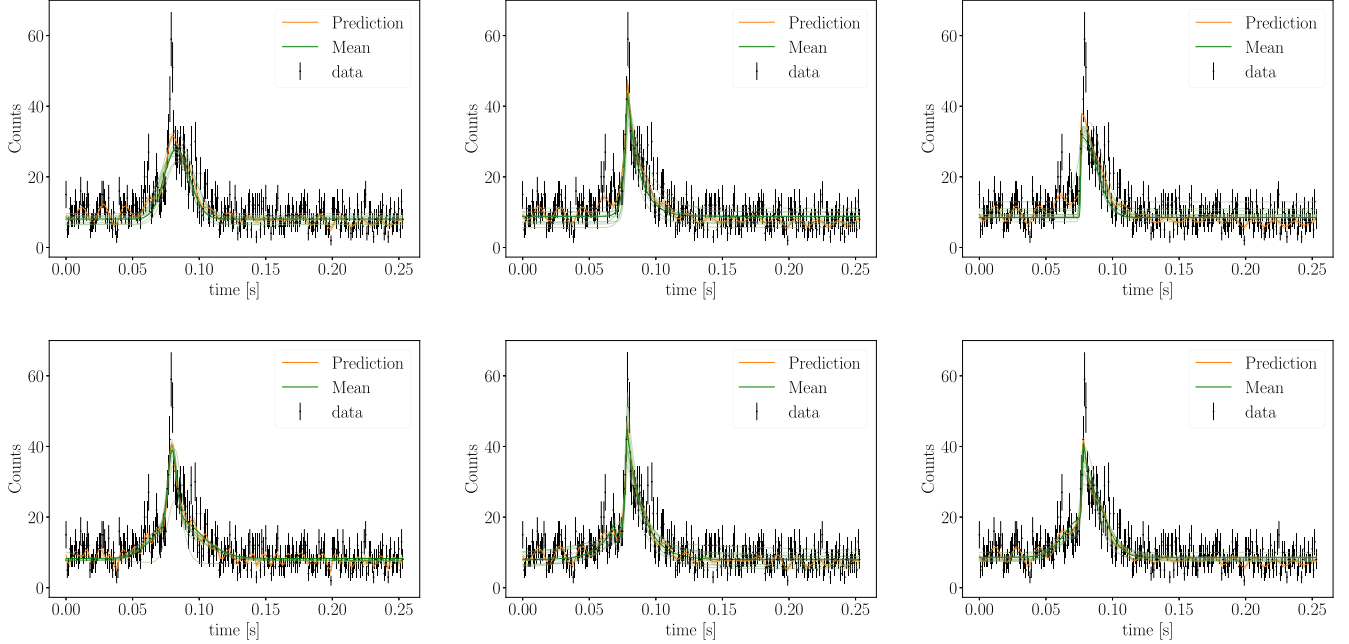


**Figure 5.** Gaussian process analysis of SGR 150228213 between  $-80$  and  $174$  ms. Different panels denote results using the  $k_{\text{qpo+rn}}$  kernel and different mean models, which contain one FRED (top left), one skewed exponential (top middle), one skewed Gaussian (top right), two FREDs (bottom left), two skewed exponentials (bottom middle), and two skewed Gaussians (bottom right). In each panel, black error bars denote the total light curve with 1 ms time resolution after zero correction, the dark green line is the mean function from the maximum likelihood sample, light green lines denote 10 other samples from the posterior, and the orange line is the prediction based on the maximum likelihood sample and the  $1\sigma$  confidence band. The energy range is 8–100 keV and the time resolution is 1 ms.

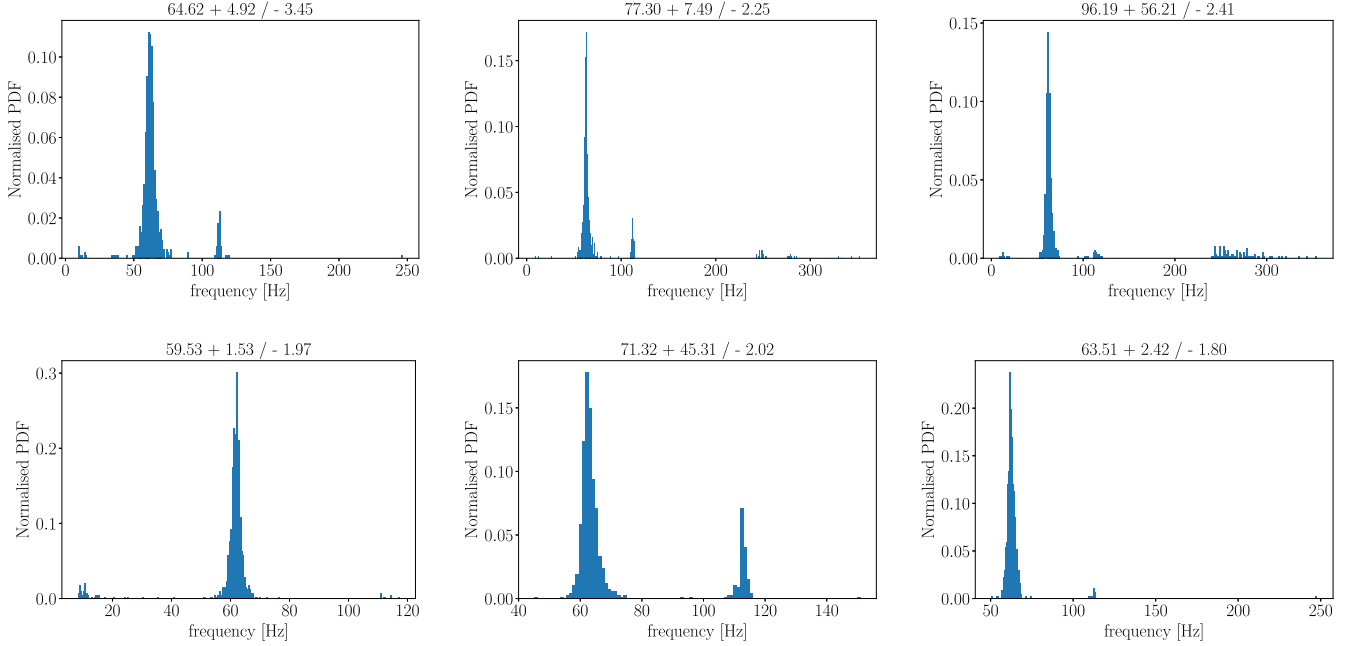


**Figure 6.** Frequency posterior distributions of SGR 150228213. Different panels denote results under different mean models, which contain one FRED (top left), one skewed exponential (top middle), one skewed Gaussian (top right), two FREDs (bottom left), two skewed exponentials (bottom middle), and two skewed Gaussians (bottom right).

**Table 3**  
Comparison of Spectral Parameters of SGR 150228213 with Bursts from 4U 0142+61<sup>a</sup>

Burst ID	Start Time in UTC (2015 Feb 28)	Blackbody + Blackbody			COMPT <sup>b</sup>			Fluence ( $10^{-8}$ erg cm $^{-2}$ )
		$kT_1$ (keV)	$kT_2$ (keV)	$\chi^2/\text{d.o.f.}$	$\alpha$	$E_p$ (keV)	$\chi^2/\text{d.o.f.}$	
1	04:53:25.023	$7.9 \pm 1.9$	$19.0 \pm 4.6$	83/64	<b><math>-0.3 \pm 0.4^c</math></b>	<b><math>53.0 \pm 5.2</math></b>	<b><math>67/65</math></b>	$12 \pm 1$
2	04:53:35.195	<b><math>2.8 \pm 0.8</math></b>	<b><math>17.6 \pm 1.2</math></b>	<b><math>55/64</math></b>	<b><math>-0.1 \pm 0.3</math></b>	<b><math>68.5 \pm 6.8</math></b>	<b><math>57/65</math></b>	$6 \pm 1$
3	04:57:21.307	<b>5.1</b>	<b><math>21.5 \pm 2.3</math></b>	<b><math>51/65</math></b>	$0.4 \pm 0.7$	$82.0 \pm 12.0$	$66/65$	$9 \pm 1$
4 <sup>d</sup>	05:06:55.645	$3.7 \pm 1.0$	$16.7 \pm 1.0$	51/64	<b><math>-0.2 \pm 0.3</math></b>	<b><math>60.6 \pm 4.6</math></b>	<b><math>47/64</math></b>	$29 \pm 2$
5	05:08:34.157	$4.6 \pm 1.3$	$23.1 \pm 8.2$	77/64	$-1.9 \pm 0.8$	$29.7 \pm 10.1$	$54/65$	$3 \pm 1$

**Notes.**

<sup>a</sup> Data collected from Göyüş et al. (2017). These bursts are analyzed in 8–200 keV. Only data from detectors with viewing angle  $\leq 40^\circ$  to source are used.

<sup>b</sup> See Section 4.2.1.

<sup>c</sup> The “preferred” model parameters for each burst are marked in bold.

<sup>d</sup> Corresponding to SGR 150228213.

location of SGR 150228213 is close to this magnetar (Roberts 2015). In addition, Swift has detected a series of hard X-ray bursts from 4U 0142+61  $\sim$ 800 s before the trigger time of SGR 150228213 (Barthelmy et al. 2015); these bursts have also been detected by Fermi/GBM.

4U 0142+61 is a prominent emitter in hard X-rays, optical, and infrared (Hulleman et al. 2004; den Hartog et al. 2008). It is the only magnetar with a debris disk but it is still debated whether it is an active gaseous one or a passive dust disk (Wang et al. 2006; Ertan et al. 2007).

For typical magnetar bursts, it is not clear whether burst spectra are predominantly thermal or nonthermal (Lin et al. 2011; van der Horst et al. 2012). Table 3 shows the spectral fitting results for short bursts from 4U 0142+61 detected by Fermi/GBM in 2015 collected from Göyüş et al. (2017). Here we select the “preferred” model for each burst following the Bayesian information criterion (BIC, Schwarz 1978), the numerical value of which is calculated from

$$\text{BIC} = -2 \ln \mathcal{L} + k \ln(\text{d.o.f.}), \quad (12)$$

where  $k$  is the number of parameters in the model, d.o.f. is the data points used in fitting, and  $\mathcal{L}$  is the maximum likelihood. When we compare the BIC of two models, if  $\Delta\text{BIC} < 6$ , we consider there is no significant preference between them, but if  $\Delta\text{BIC} > 6$ , we prefer the model with smaller BIC (Jeffreys 1939; Mukherjee et al. 1998).

The “preferred” model parameters for each burst are marked in bold in Table 3. According to the results from fitting of the energy spectrum, SGR 150228213 is not significantly different from other bursts from 4U 0142+61. Moreover these short bursts from 4U 0142+61 detected in 2015 mostly have a harder energy spectrum than “regular” bursts from short magnetars (which usually have  $E_p$  below 50 keV in COMPT model fitting), which may indicate different physical origins of these bursts. Unfortunately, we did not find any QPOs similar to SGR 150228213 in other bursts from 4U 0142+61, which may

be because the burst intensities are too low to provide sufficient significance for the potential QPOs.

Combined with the relationship for the active phase of 4U 0142+61 and location, 4U 0142+61 is undoubtedly the most likely origin of SGR 150228213. If this QPO signal is not a false detection, it would be the first observation of QPOs in bursts from AXPs. Considering the special feature of 4U 0142+61 itself, it may bring us a new perspective on the burst mechanism of this magnetar.

## 4.2. The Relation between SGR 150228213 and FRB 180916

Since SGR 150228213 is associated with FRB 180916 on location, we try to discuss the different origins of SGR 150228213 from a more interesting perspective.

FRB 180916 is an active repeating FRB source with a period of  $\sim 16.35 \pm 0.15$  days and a phase window of 5 days (CHIME/FRB Collaboration et al. 2020). It was localized to a star-forming region in a nearby massive spiral galaxy at redshift  $z \sim 0.0337 \pm 0.0002$  (Marcote et al. 2020). If this connection exists, SGR 150228213 may be a short GRB event generated from a newborn magnetar, which can also explain the highly active features of FRB 180916.

### 4.2.1. Spectral Analysis and the Amati Relation

If we treat SGR 150228213 as a possible short GRB, we can use the Amati relation (Amati 2006) to check whether it is correlated with the trend of short GRBs based on analysis of its energy spectrum. In this case, we used the COMPT model and the multicolor blackbody (mBB) model to fit the energy spectrum of SGR 150228213 between 8 keV and 40 MeV, and check which model fits the burst better to compute its fluence. We extract the source spectra and background spectra, and generate the instrumental response matrix from the detectors n4, n8, and b0. All spectra are fitted using Xspec (Arnaud 1996). We use the maximum likelihood for Poisson data with

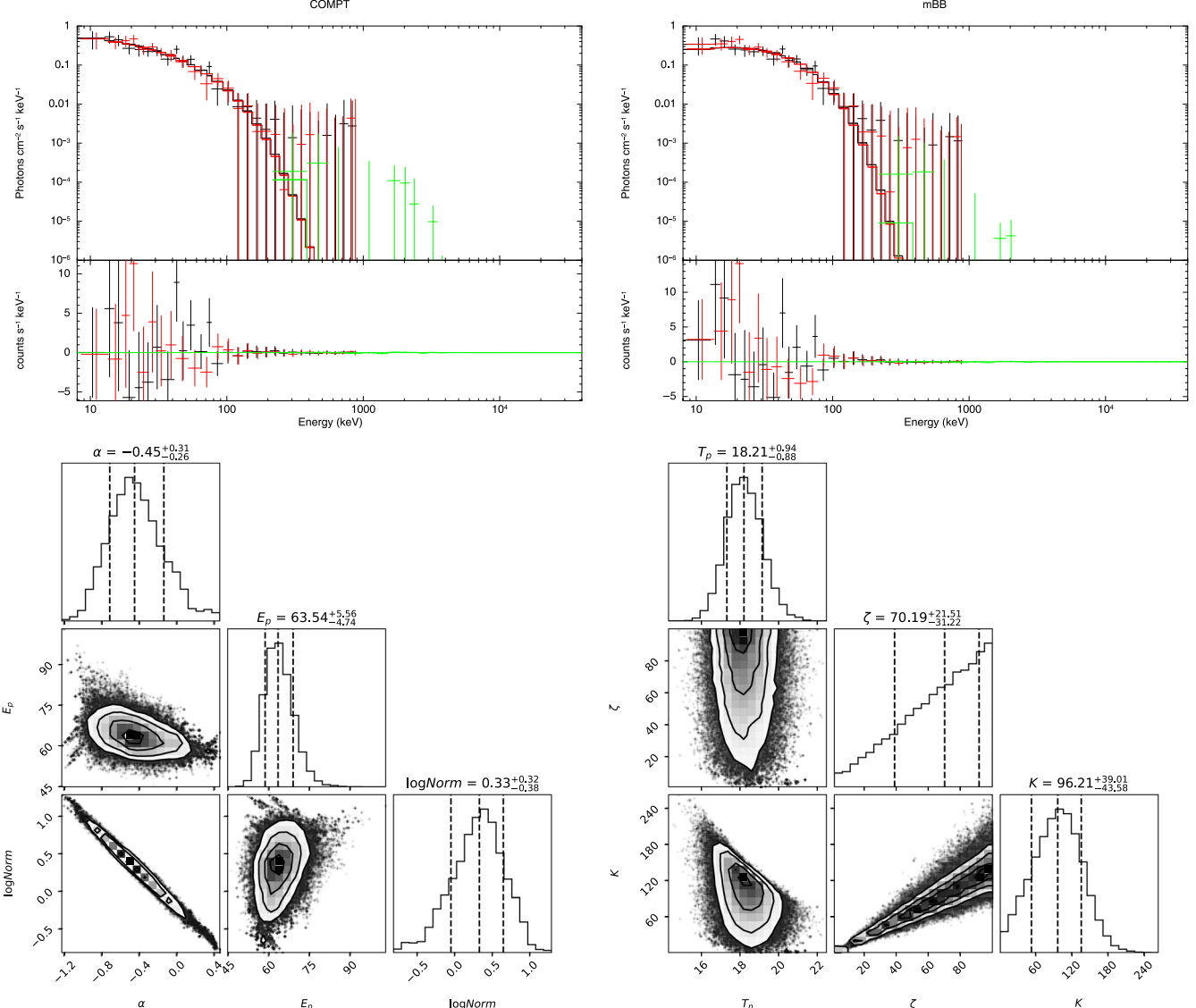


**Figure 7.** Time-integrated spectral fitting results in 8–40,000 keV. Spectra of the counts in the COMPT model (top left) and mBB model (top right) are drawn with their residuals. The likelihood maps of free parameters in COMPT (bottom left) and mBB (bottom right) have been marked with their  $1\sigma$  uncertainties.

Gaussian background to estimate the best-fit parameters and choose the optimum model parameters through the MCMCs.

The COMPT model is defined as

$$N(E) = KE^\alpha \exp[-(\alpha + 2)E/E_p], \quad (13)$$

where  $K$  is the normalization factor,  $\alpha$  is the photon index, and  $E_p$  is the peak energy in the  $\nu F_\nu$  spectrum. The mBB model we used corresponds to `diskpbb` in Xspec, and it is defined as (Iyyani & Sharma 2021)

$$N(E) = \frac{4\pi E^2}{h^2 c^2} \left( \frac{K}{\zeta} \right) T_p^{2/\zeta} \int_{T_{\min}}^{T_p} \frac{T^{-(2+\zeta)/\zeta}}{e^{E/T} - 1} dT, \quad (14)$$

where  $K$  is the normalization factor,  $\zeta$  is the power-law index of the radial dependence of temperature ( $T(r) \propto r^{-\zeta}$ ),  $T_p$  is the peak temperature in keV, and  $T_{\min}$  is the minimum temperature of the underlying blackbodies and is considered to be well below the energy range of the observed data.

The spectrum of SGR 150228213 and the model fitting results are presented in Figure 7. According to these results, the nonthermal origin of SGR 150228213 is supported further and we can use the COMPT model fitting results to compute  $E_{\gamma,\text{iso}}$  of SGR 150228213 as  $\sim 1.25 \times 10^{48}$  erg based on the redshift of FRB 180916.

According to the Amati relation, the correlation between isotropic bolometric emission energy ( $E_{\gamma,\text{iso}}$ ) and the rest-frame

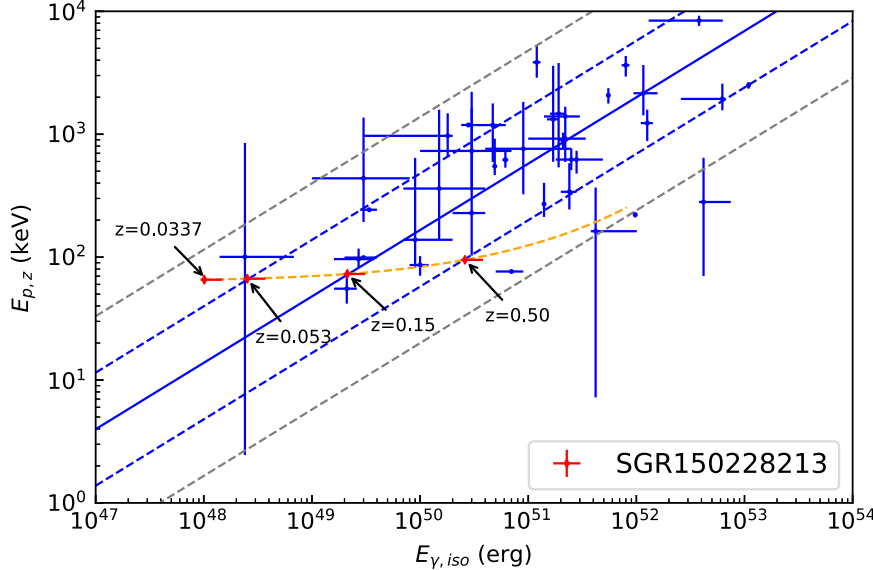


**Figure 8.** SGR 150228213 in the  $E_{p,z}$ - $E_{\gamma,\text{iso}}$  correlation diagram of short GRBs. The blue solid line denotes the relation for short GRBs, and the blue and gray dashed lines denote the  $1\sigma$  and  $2\sigma$  regions. The orange dashed line denotes the position of SGR 150228213 if its redshift were taken from 0.0337 to 3. Red diamonds denote the position of SGR 150228213 at  $z = 0.0337$  (the redshift of FRB 180916),  $z = 0.15$  (the “best” position for SGR 150228213 in current correlation for short GRBs),  $z = 0.053$ , and  $z = 0.5$ . Other data on short GRBs are taken from Zhang et al. (2009) and Wang et al. (2018b). The best correlation of short GRBs is taken as  $\log(E_p/\text{erg}) = (3.24 \pm 0.07) + (0.54 \pm 0.04)\log(E_{\gamma,\text{iso}}/10^{52} \text{ erg})$  (Zhang et al. 2018).

peak energy ( $E_{p,z}$ ) could be written as

$$\frac{E_{p,z}}{100 \text{ keV}} = C \left( \frac{E_{\gamma,\text{iso}}}{10^{52} \text{ erg}} \right)^m, \quad (15)$$

where  $C$  is around 0.8–1 and  $m$  is around 0.4–0.6. This relation is initially found in long GRBs with known redshifts, but similar relations for short GRBs have also been found in later works (Ghirlanda et al. 2009; Zhang et al. 2009).

Figure 8 is the  $E_{p,z}$ - $E_{\gamma,\text{iso}}$  diagram of short GRBs. The position of SGR 150228213 at  $z = 0.0337$  is within the  $1\sigma$  to  $2\sigma$  error region of the distribution of short GRBs, and the “best” redshift range for SGR 150228213 corresponding to short GRBs is  $z = 0.15^{+0.35}_{-0.097}$ .

#### 4.2.2. Chance Probability

Apart from the possibility of verifying SGR 150228213 as a short GRB from the Amati relation, we need to estimate the chance probability of the association between FRB 180916 and SGR 150228213. However, the calculation may suffer from some uncertainties. Nevertheless, we simply assume that SGR 150228213 is a candidate for a short GRB associated with FRB 180916. Following the methods in Wang et al. (2020), the chance probability of the association may be calculated as

$$P = 1 - \lambda^0 \exp(-\lambda)/0! = 1 - \exp(-\lambda), \quad (16)$$

where  $\lambda = \rho S$  is the number of FRBs in the region  $S$  ( $\approx [41,252.96(1 - \cos \delta R)]/2$ ). The surface number density

of our FRB samples is  $\rho \approx 626/41,252.96 \approx 0.015 \text{ deg}^{-2}$ . For the centering angular distance from FRB 180916 to SGR 150228213  $\delta R \sim 0^\circ.4975$ , one gets the chance probability  $\sim 1.16\%$ .<sup>7</sup> It can be seen that the chance probability of  $\sim 1\%$  is relatively slight, which implies the possibility of association, but it is not significant. Therefore, combined with the physical analysis in the previous section, we leave open the possibility of a true association between SGR 150228213 and FRB 180916.

## 5. Summary

We applied a Bayesian framework to the observed periodogram of SGR 150228213 based on the assumption that all broadband power in a periodogram comes from the noise process without QPOs. We detected a narrow QPO at 112.20 Hz with a width of 5.64 Hz and a wide QPO at 57.54 Hz with a width of 26.48 Hz in SGR 150228213, with a significance level of 0.0004 (corresponding to a confidence level  $\simeq 3.35\sigma$ ).

We have also discussed the possible origins of SGR 150228213, and consider that it most likely comes from the known magnetar 4U 0142+61. If it indeed comes from 4U 0142+61, this would be the first detection of QPOs in bursts from AXPs, which may lead to new insights into the physical

<sup>7</sup> However, if one takes  $\delta R \sim 5^\circ.45$  as the radius of the position error circle (with 90% confidence) of SGR 150228213, then one gets a much higher chance probability  $\sim 24.69\%$ .

mechanisms of magnetar bursts. However, we still do not rule out the possibility that it is a short GRB associated with FRB 180916.

### Acknowledgments

We acknowledge the use of the Fermi archive public data. This work is supported by the National Natural Science Foundation of China (grant Nos. 12203013, 12273005, and U1938201), China Manned Spaced Project (CMS-CSST-2021-B11), and the Guangxi Science Foundation (grant Nos. AD22035171 and 2023GXNSFBA026030).

### References

- Amati, L. 2006, *MNRAS*, **372**, 233
- Arnaud, K. A. 1996, in ASP Conf. Ser. 101, Astronomical Data Analysis Software and Systems V, ed. G. H. Jacoby & J. Barnes (San Francisco, CA: ASP), 17
- Barat, C., Hayles, R. I., Hurley, K., et al. 1983, *A&A*, **126**, 400
- Barthelmy, S. D., Gehrels, N., Kennea, J. A., et al. 2015, GCN, 17507, 1
- Belli, B. M. 1992, *ApJ*, **393**, 266
- Bochenek, C. D., Ravi, V., Belov, K. V., et al. 2020, *Natur*, **587**, 59
- Cameron, P. B., Chandra, P., Ray, A., et al. 2005, *Natur*, **434**, 1112
- Castro-Tirado, A. J., Østgaard, N., Görgüç, E., et al. 2021, *Natur*, **600**, 621
- Cline, T. L., Desai, U. D., Pizzichini, G., et al. 1980, *ApJL*, **237**, L1
- CHIME/FRB Collaboration, Amiri, M., Andersen, B. C., et al. 2020, *Natur*, **582**, 351
- CHIME/FRB Collaboration, Amiri, M., Andersen, B. C., et al. 2021, *ApJS*, **257**, 59
- CHIME/FRB Collaboration, Andersen, B. C., Bandura, K. M., et al. 2020, *Natur*, **587**, 54
- den Hartog, P. R., Kuiper, L., Hermsen, W., et al. 2008, *A&A*, **489**, 245
- Duncan, R. C., & Thompson, C. 1992, *ApJL*, **392**, L9
- Ertan, Ü., Erkut, M. H., Eksı, K. Y., & Alpar, M. A. 2007, *ApJ*, **657**, 441
- Feroci, M., Frontera, F., Costa, E., et al. 1999, *ApJL*, **515**, L9
- Foreman-Mackey, D., Hogg, D. W., Lang, D., & Goodman, J. 2013, *PASP*, **125**, 306
- Gaensler, B. M., Kouveliotou, C., Gelfand, J. D., et al. 2005, *Natur*, **434**, 1104
- Ghirlanda, G., Nava, L., Ghisellini, G., Celotti, A., & Firmani, C. 2009, *A&A*, **496**, 585
- Görgüç, E., Lin, L., Roberts, O. J., et al. 2017, *ApJ*, **835**, 68
- Groth, E. J. 1975, *ApJS*, **29**, 285
- Hübner, M., Huppenkothen, D., Lasky, P. D., et al. 2022, *ApJ*, **936**, 17
- Hulleman, F., van Kerwijk, M. H., & Kulkarni, S. R. 2004, *A&A*, **416**, 1037
- Huppenkothen, D., Bachetti, M., Stevens, A. L., et al. 2019, *ApJ*, **881**, 39
- Huppenkothen, D., Brewer, B. J., Hogg, D. W., et al. 2015, *ApJ*, **810**, 66
- Huppenkothen, D., D'Angelo, C., Watts, A. L., et al. 2014c, *ApJ*, **787**, 128
- Huppenkothen, D., Heil, L. M., Watts, A. L., & Görgüç, E. 2014a, *ApJ*, **795**, 114
- Huppenkothen, D., Watts, A. L., & Levin, Y. 2014b, *ApJ*, **793**, 129
- Huppenkothen, D., Watts, A. L., Uttley, P., et al. 2013, *ApJ*, **768**, 87
- Hurley, K., Boggs, S. E., Smith, D. M., et al. 2005, *Natur*, **434**, 1098
- Hurley, K., Cline, T., Mazets, E., et al. 1999, *Natur*, **397**, 41
- Israel, G. L., Belloni, T., Stella, L., et al. 2005, *ApJL*, **628**, L53
- Iyyani, S., & Sharma, V. 2021, *ApJS*, **255**, 25
- Jeffreys, H. 1939, Theory of Probability (Oxford: Oxford Univ. Press)
- Kaspi, V. M., & Beloborodov, A. M. 2017, *ARA&A*, **55**, 261
- Katz, J. I. 2016, *ApJ*, **826**, 226
- Kouveliotou, C., Meegan, C. A., Fishman, G. J., et al. 1993, *ApJL*, **413**, L101
- Lazzati, D. 2002, *MNRAS*, **337**, 1426
- Leahy, D. A., Darbro, W., Elsner, R. F., et al. 1983, *ApJ*, **266**, 160
- Li, C. K., Lin, L., Xiong, S. L., et al. 2021, *NatAs*, **5**, 378
- Li, X., Ge, M., Lin, L., et al. 2022, *ApJ*, **931**, 56
- Lin, L., Görgüç, E., Roberts, O. J., et al. 2020a, *ApJ*, **893**, 156
- Lin, L., Zhang, C. F., Wang, P., et al. 2020b, *Natur*, **587**, 63
- Lin, L., Kouveliotou, C., Baring, M. G., et al. 2011, *ApJ*, **739**, 87
- Lomb, N. R. 1976, *Ap&SS*, **39**, 447
- Lyubarsky, Y. 2014, *MNRAS*, **442**, L9
- Lyubarsky, Y. 2021, *Universe*, **7**, 56
- Marcote, B., Nimmo, K., Hessels, J. W. T., et al. 2020, *Natur*, **577**, 190
- Mazets, E. P., Cline, T. L., Aptekar, R. L., et al. 1999, *AstL*, **25**, 635
- Mazets, E. P., Golentskii, S. V., Ilinskii, V. N., Aptekar, R. L., & Guryan, I. A. 1979, *Natur*, **282**, 587
- Meegan, C., Lichti, G., Bhat, P. N., et al. 2009, *ApJ*, **702**, 791
- Mereghetti, S., Savchenko, V., Ferrigno, C., et al. 2020, *ApJL*, **898**, L29
- Miller, M. C., Chirenti, C., & Strohmayer, T. E. 2019, *ApJ*, **871**, 95
- Mukherjee, S., Feigelson, E. D., Jogesh Babu, G., et al. 1998, *ApJ*, **508**, 314
- Norris, J. P., Nemiroff, R. J., Bonnell, J. T., et al. 1996, *ApJ*, **459**, 393
- Olausen, S. A., & Kaspi, V. M. 2014, *ApJS*, **212**, 6
- Palmer, D. M., Barthelmy, S., Gehrels, N., et al. 2005, *Natur*, **434**, 1107
- Petroff, E., Barr, E. D., Jameson, A., et al. 2016, *PASA*, **33**, e045
- Ridnaia, A., Svinkin, D., Frederiks, D., et al. 2021, *NatAs*, **5**, 372
- Roberts, O. J. 2015, GCN, 17508, 1
- Roberts, O. J., Veres, P., Baring, M. G., et al. 2021, *Natur*, **589**, 207
- Scargle, J. D. 1982, *ApJ*, **263**, 835
- Scargle, J. D., Norris, J. P., Jackson, B., & Chiang, J. 2013, *ApJ*, **764**, 167
- Schwarz, G. 1978, *AnSta*, **6**, 461
- Strohmayer, T. E., & Watts, A. L. 2005, *ApJL*, **632**, L111
- Strohmayer, T. E., & Watts, A. L. 2006, *ApJ*, **653**, 593
- Svinkin, D., Frederiks, D., Hurley, K., et al. 2021, *Natur*, **589**, 211
- Thompson, C., & Duncan, R. C. 1995, *MNRAS*, **275**, 255
- Timmer, J., & Koenig, M. 1995, *A&A*, **300**, 707
- Turolla, R., Zane, S., & Watts, A. L. 2015, *RPPh*, **78**, 116901
- van der Horst, A. J., Kouveliotou, C., Gorgone, N. M., et al. 2012, *ApJ*, **749**, 122
- Vaughan, S. 2010, *MNRAS*, **402**, 307
- Wang, W., Luo, R., Yue, H., et al. 2018a, *ApJ*, **852**, 140
- Wang, X.-G., Zhang, B., Liang, E.-W., et al. 2018b, *ApJ*, **859**, 160
- Wang, X.-G., Li, L., Yang, Y.-P., et al. 2020, *ApJL*, **894**, L22
- Wang, Z., Chakrabarty, D., & Kaplan, D. L. 2006, *Natur*, **440**, 772
- Xiao, S., Peng, W.-X., Zhang, S.-N., et al. 2022, *ApJ*, **941**, 166
- Yang, J., Chand, V., Zhang, B.-B., et al. 2020, *ApJ*, **899**, 106
- Yang, Y.-H., Zhang, B.-B., Lin, L., et al. 2021, *ApJL*, **906**, L12
- Yang, Y.-P., & Zhang, B. 2018, *ApJ*, **868**, 31
- Yu, Y.-W., Zou, Y.-C., Dai, Z.-G., & Yu, W.-F. 2021, *MNRAS*, **500**, 2704
- Zhang, B., Zhang, B.-B., Virgili, F. J., et al. 2009, *ApJ*, **703**, 1696
- Zhang, B. B., Zhang, B., Sun, H., et al. 2018, *NatCo*, **9**, 447
- Zhang, H.-M., Liu, R.-Y., Zhong, S.-Q., & Wang, X.-Y. 2020, *ApJL*, **903**, L32